Results in Surfaces and Interfaces 24 (2026) 100864

Contents lists available at ScienceDirect

Results in Surfaces and Interfaces

journal homepage: www.elsevier.com/locate/rsurfi

Molecular dynamics study on the mechanical properties, fracture toughness and crack propagation behavior of polycrystalline B_6N_6, BN, BC_3, and C_3N_4 nanosheets

Morteza Ghorbanzadeh Ahangari [*], Mostafa Fathalian, Sajjad Dargahi

Department of Mechanical Engineering, Faculty of Engineering and Technology, University of Mazandaran, Babolsar, Iran

ARTICLE INFO

Keywords:
Polycrystalline nanosheets
Nanotubes
Mechanical properties
Fracture toughness
Crack propagation

ABSTRACT

This study employs molecular dynamics simulations to examine the mechanical properties, fracture toughness, and crack propagation behavior of polycrystalline B_6N_6, BN, BC_3, and C_3N_4 nanosheets and nanotubes. The effects of the number of grains, temperature, strain rate, edge pre-cracks, and circular-notch defects on Young's modulus, tensile strength, failure strain, and critical fracture toughness is systematically analyzed. Results show that increasing the number of grains reduces both tensile strength and Young's modulus, with BN nanosheets demonstrating the highest overall mechanical performance. Polycrystalline B_6N_6 exhibits the greatest fracture toughness, followed by BN, BC_3, and C_3N_4, reflecting the role of atomic structure and bonding in energy absorption before failure. Thermal analysis indicates that BN maintains superior mechanical stability at elevated temperatures due to reduced atomic vibrations and stronger B–N bonds. Analyses of pre-cracks and notches reveal that BN is most sensitive to crack propagation, whereas BC_3 and C_3N_4 show crack-insensitive behavior, with failure often initiating at grain boundaries rather than crack tips. Strain rate effects suggest that higher rates enhance fracture toughness by limiting atomic rearrangements and crack growth. For nanotubes, increasing diameter enhances Young's modulus but reduces tensile strength, failure strain, and fracture toughness, with C_3N_4 nanotubes being most sensitive to temperature. These findings provide detailed insights into the mechanical behavior of polycrystalline nanosheets and nanotubes, guiding the design of nanomaterials with optimized strength, toughness, and thermal stability for advanced applications.

1. Introduction

Two-dimensional (2D) materials, despite their atomic-scale thickness and nanometer-to-micrometer lateral dimensions, rarely exist as perfect single crystals in practical applications. Instead, the reality of synthesis, whether through chemical vapor deposition, exfoliation, or solution processing, inevitably produces polycrystalline architectures characterized by grain boundaries, phase interfaces, and various atomic-scale defects [1,2]. These structural features fundamentally alter the physical, chemical, and electronic properties that make 2D materials attractive for advanced technologies [3]. While pristine graphene showcased the theoretical potential of atomically thin semiconductors, it's the polycrystalline versions of graphene and alternative 2D materials, hexagonal boron nitride (h-BN), boron-carbon-nitrogen compounds (BC_3, BC_6N), boron-nitride derivatives (B_6N_6), and carbon nitride allotropes (C_3N, C_3N_4), that dominate real-world applications in electronics, photocatalysis, and structural nanocomposites. Specifically, BN nanosheets are widely used in high-temperature electronics, thermal management systems, and protective coatings due to their exceptional mechanical strength and thermal stability. B_6N_6 offers superior fracture toughness, making it suitable for impact-resistant nanocomposites and energy-absorbing structures. BC_3 is explored for flexible electronics and optoelectronic devices owing to its tunable electronic properties. C_3N_4, known for its photocatalytic activity, is extensively applied in water splitting, hydrogen production, and environmental remediation [4–8].

The distinction matters more than one might initially assume. Polycrystalline 2D materials exhibit band gaps ranging from 0.39 eV (C_3N) to 2.76 eV (graphitic C_3N_4), but these values shift considerably depending on grain size distribution and boundary structure [6–8]. Graphitic C_3N_4, with its layered hexagonal lattice of tri-s-triazine units, demonstrates notable photocatalytic properties that actually benefit from certain grain boundary configurations, an

---

* Corresponding author.
E-mail addresses: m.ghorbanzadeh@umz.ac.ir, ghorbanzadeh.morteza@gmail.com (M.G. Ahangari).

https://doi.org/10.1016/j.rsurfi.2026.100864
Received 15 February 2026; Received in revised form 26 May 2026; Accepted 4 June 2026
Available online 5 June 2026
2666-8459/© 2026 The Authors. Published by Elsevier B.V. This is an open access article under the CC BY license (http://creativecommons.org/licenses/by/4.0/).

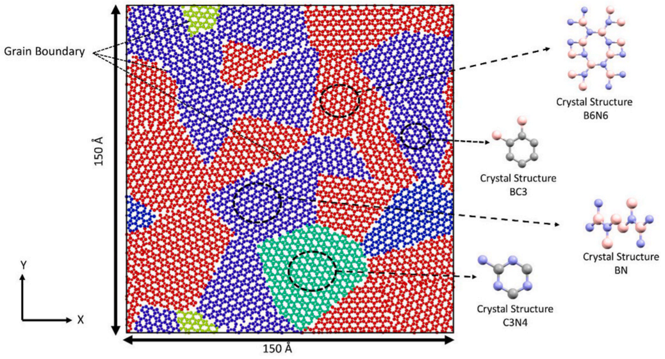

Fig. 1. Schematic of polycrystalline B_6N_6, BN, BC_3, and C_3N_4 nanosheets showing crystal structures, dimensions, and grain boundaries.

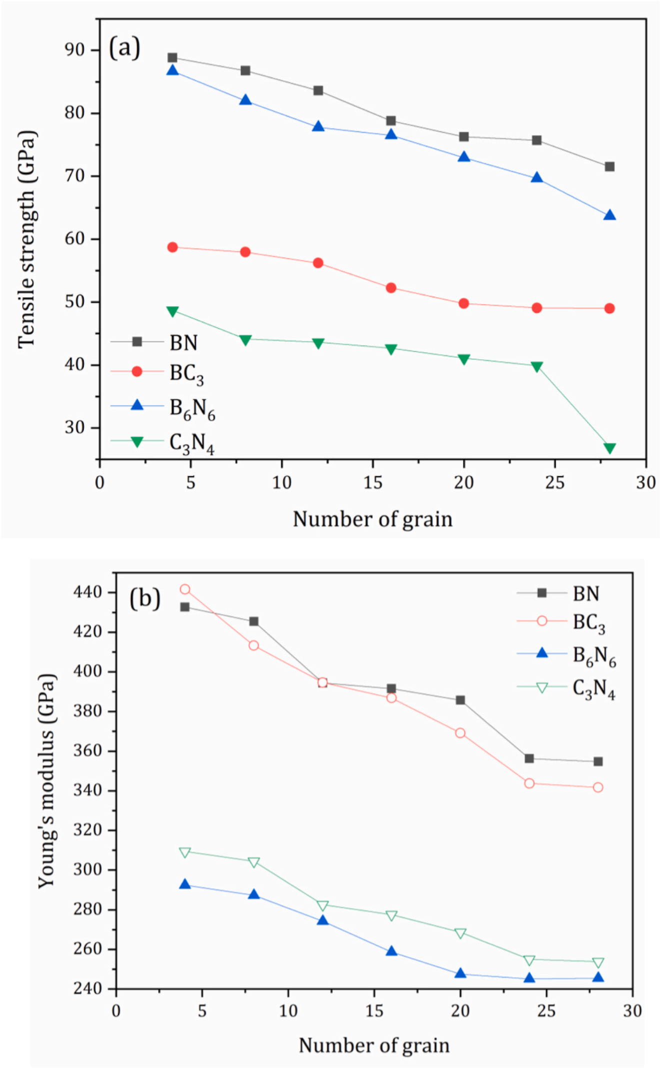

Fig. 2. Mechanical properties, including (a) tensile strength ad (b) Young's modulus, with respect to the number of grains for polycrystalline B_6N_6, BC_3, BN, and C_3N_4 nanosheets.

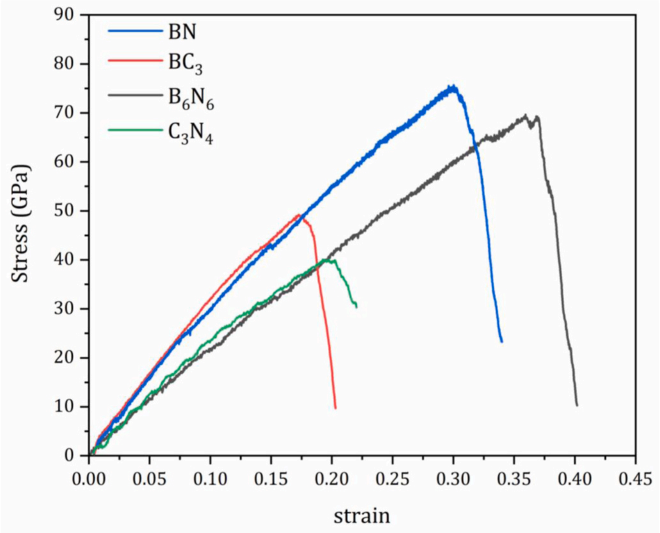

Fig. 3. The stress–strain curves of polycrystalline nanosheets with 24 grains.

unexpected finding that challenges the common assumption that defects always degrade performance [9–12]. That said, C_3N's superior mechanical characteristics, which can rival graphene in specific contexts, deteriorate rapidly once polycrystallinity is introduced [13,14]. The grain boundaries act as weak links, stress concentrators, and sometimes even as preferential crack propagation paths. Grain boundaries not only reduce strength, but they also fundamentally alter deformation mechanisms. Grain boundaries act as stress concentrators, scattering centers for phonons and electrons, and preferential sites for crack initiation. Molecular dynamics (MD) simulation is a computational method that models the motion of atoms and molecules by solving Newton's equations of motion. In composite materials and metal alloys, MD helps reveal how atomic interactions influence mechanical strength and thermal behavior, providing insight into properties such as elasticity, fracture resistance, heat conduction, and overall stability [15–17] Mortazavi and Cuniberti [18] demonstrated this through pioneering MD studies on ultrafine grained single-layer boron-nitride films, showing that decreasing grain size from moderate to ultra-fine scales gradually reduced elastic modulus, with ultrafine-grained samples showing tensile strength approximately half that of their pristine counterparts. Interestingly, the relationship is not linear; there's a threshold effect where grain refinement beyond a certain point triggers catastrophic weakening. Similar patterns were reported in Chen et al. [19] investigated polycrystalline graphene, where reducing grain size from 2.5 nm to 10 nm decreased Young's modulus and failure strength while paradoxically increasing failure strain, presumably because smaller grains allow more distributed deformation before catastrophic failure.

Temperature compounds these issues in ways that aren't always intuitive. Chen's work showed that increasing the temperature from 100 K to 1200 K reduced the failure strength by approximately 45% in polycrystalline graphene; however, the degradation wasn't uniform across grain sizes [20]. Polycrystalline variants proved far more sensitive to both temperature and strain rate than single crystals. At room temperature, increasing the strain rate enhanced failure strength by roughly 10%, suggesting that dynamic loading conditions might partially offset grain boundary weakening effects. Whether this holds for other 2D polycrystals remains an open question.

The chemistry of grain boundaries adds another layer of complexity. Elapolu and Tabarraei's investigation of hydrogenated grain boundaries in polycrystalline graphene revealed that increased hydrogenation significantly reduces stiffness, no surprise there, but that failure strength remains relatively unaffected initially [21].

Defect sensitivity in polycrystalline architectures follows non-obvious patterns. Also, defect healing and interlayer engineering could mitigate mechanical degradation [21,22]. Shirazi et al. [20] demonstrated that C_3N nanosheets with pre-existing cracks and notches show a Young's modulus declining approximately 9% over 200–900 K, with ultimate tensile strength plummeting as crack length increases. In

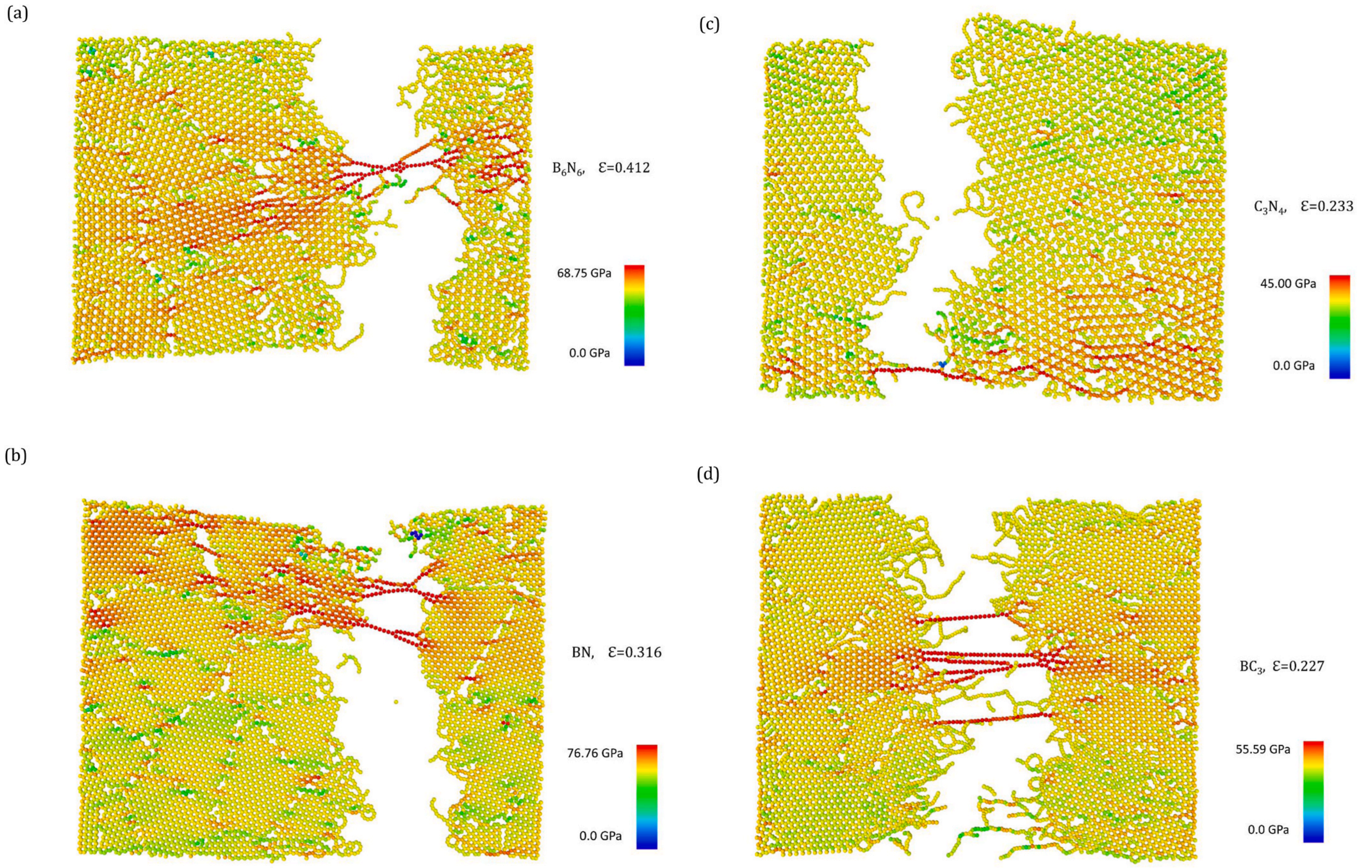

Fig. 4. Ruptured configurations of polycrystalline (a) B_6N_6, (b) BN, (c) C_3N_4, and (d) BC_3 with 24 grains under failure strain.

parallel studies of BC_3, defect-free samples exhibited a higher elastic modulus along the zigzag direction, but once polycrystallinity was introduced, directionality effects weakened considerably, as grain boundaries essentially randomize what would otherwise be crystallographic preferences [23–25]. The stiffer C-N bonds (770 kcal/mol) versus C-B bonds (448 kcal/mol) mean C_3N retains superior elastic modulus even when defective, but only if grain boundaries don't dominate the failure mechanism.

Despite substantial progress on individual material systems through isolated studies, systematic comparative investigations across polycrystalline B_6N_6, BN, BC_3, and C_3N_4 nanosheets remain surprisingly scarce. To establish a systematic framework for investigating the mechanical response of two-dimensional boron–carbon–nitrogen (B–C–N) nanosheets, the present study focuses on four specific compositions: BN, B_6N_6, BC_3, and C_3N_4. The selection follows a defined rationale based on two orthogonal compositional axes: carbon concentration and boron presence. BN serves as the carbon-free reference, representing the baseline mechanical behavior of hexagonal boron nitride. B_6N_6, despite being also stoichiometric BN, exhibits a distinct ring topology, enabling the assessment of configurational effects independent of carbon incorporation. BC_3 introduces carbon-rich substitution (B:C molar ratio of 1:3), allowing systematic evaluation of carbon-induced modifications in fracture toughness and crack dynamics. C_3N_4, in which boron is fully replaced by carbon while maintaining nitrogen (C:N = 3:4), isolates the influence of boron depletion under carbon-dominant stoichiometry. Collectively, these four systems span a compositional continuum from carbon-free (BN) to carbon-rich (BC_3) and boron-free (C_3N_4) regimes, thereby enabling a comparative evaluation of how incremental variations in chemical composition govern the mechanical properties, fracture toughness, and crack propagation behavior of polycrystalline B–C–N nanosheets.

This study addresses the existing gaps through comprehensive MD simulations [26,27], systematically examining tensile strength, Young's modulus, failure strain, fracture toughness, and crack propagation behavior across polycrystalline B_6N_6, BN, BC_3, and C_3N_4 nanosheets with varying grain numbers (4–28 grains), temperatures spanning 100–1500 K, defect configurations including edge pre-cracks and circular notches, and strain rates in the range of 2.5×10^6–2.5×10^9 s^{-1}. The analysis is further extended to nanotubes with diameters ranging from 12.7 to 31.8 Å, establishing a comparative framework that elucidates the specific deformation and failure mechanisms governing these materials, mechanisms essential for designing next-generation high-temperature electronics, protective coatings, energy storage devices, and high-strength nanocomposites that must function with realistic, polycrystalline microstructures rather than idealized single crystals.

2. Computational method and modelling approach

MD simulations were conducted using the Large-scale Atomic/Molecular Massively Parallel Simulator (LAMMPS) package [27–29], to investigate the mechanical and fracture properties of polycrystalline nanosheets (PCSs) and polycrystalline nanotubes (PCNs) composed of BN, BC_3, B_6N_6, and C_3N_4. Atomic interactions were modeled using the optimized Tersoff potential, as specified by Kinaci et al. [28], which is well-validated for describing bonding in boron-nitride and carbon-based systems, including BN-C hybrid nanostructures.

PCSs of BN, BC_3, B_6N_6, and C_3N_4 were generated using the AtomSK software package [30]. The Voronoi tessellation method was employed to create polycrystalline structures with controlled grain counts ranging from 4 to 28 grains. In this approach, seed points are randomly distributed on a planar domain, and the region is partitioned into grains corresponding to the Voronoi cells of these seeds. Each grain was assigned a random crystallographic orientation, and grain boundaries consisting of pentagon-heptagon defect rings were introduced at the

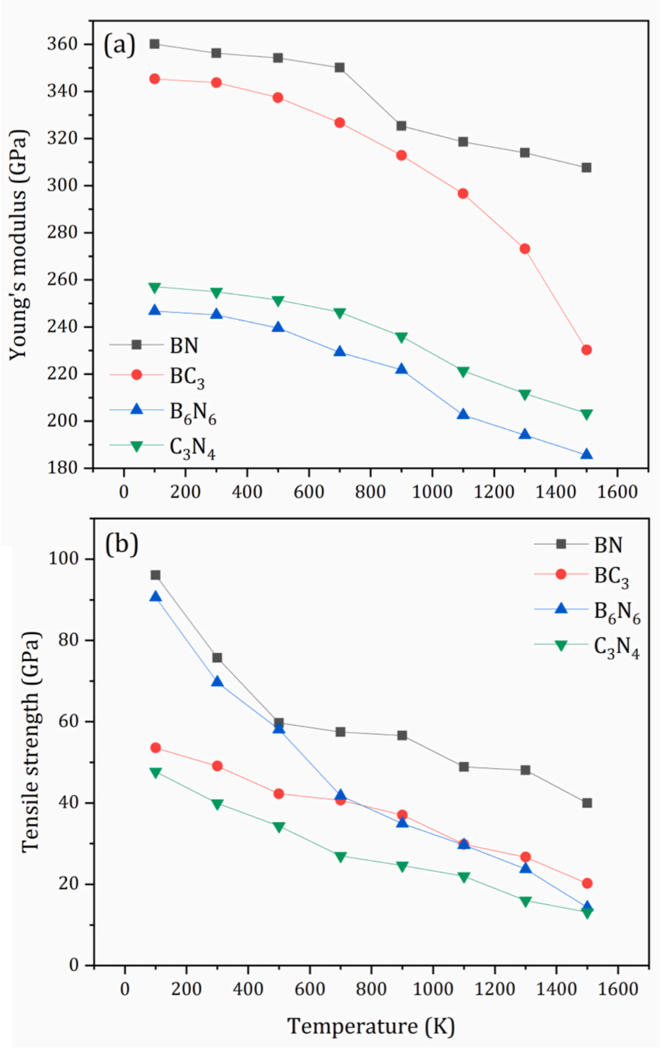

Fig. 5. (a) Young's modulus and (b)tensile strength with respect to temperature for polycrystalline BN, BC_3, C_3N_4, and B_6N_6 nanosheets.

interfaces between adjacent grains. The dimensions of the nanosheets were approximately 150 × 150 Å^2, with periodic boundary conditions applied in the in-plane directions.

Polycrystalline nanotubes were produced by rolling the pre-generated PCSs into cylindrical geometries. Specifically, the flat PCS was rolled up along a chosen direction to form a nanotube with a specified diameter. The rolling direction was selected perpendicular to the grain boundary orientation to preserve the grain topology on the cylindrical surface. This two-step approach, first generating a PCS on a flat surface and then rolling it into a tube, avoids the geometric complexity of applying Voronoi tessellation directly onto a curved surface, while ensuring that grain boundaries remain physically realistic. Nanotubes with diameters ranging from 12.7 to 31.8 Å and a constant length of 50 Å were generated for all samples. The samples were initially equilibrated at room temperature (300 K) using the (NVT) ensemble to ensure structural stability. Uniaxial tensile tests were performed on the nanosheets along the x-directions at strain rates ranging from 2.5×10^6 to 2.5×10^9 s^{-1}. It is well recognized that the calculated Young's modulus of samples depends on the assumed wall thickness. In the present study, the wall thickness was taken as twice the bond length: 2.9 Å for BN and B_6N_6 (based on the B–N bond length), 3.14 Å for BC_3 (based on the B–C bond length), and 2.74 Å for C_3N_4 (based on the C–N bond length) [31]. To explore temperature effects, simulations were conducted at temperatures of 100-1500 K, maintained using a Nose-Hoover thermostat with a simulation timestep of 0.5 fs. To assess the impact of structural defects on fracture properties, cracks were introduced into the nanosheets by selectively removing atoms along predefined lengths and widths. The tensile testing protocol for defective samples mirrored that of pristine structures, enabling direct comparisons of stress-strain responses and failure mechanisms. Atomic configurations and deformation mechanisms for both nanosheets and nanotubes were visualized using the Open Visualization Tool (OVITO) [29].

Fig. 1 illustrates the schematic representation of the PCSs modeled in this study, including the crystal structures of B_6N_6, BN, BC_3, and C_3N_4. The figure shows their characteristic atomic arrangements, along with the dimensions of the nanosheets used in simulations.

3. Results and discussion

The effect of the number of grains, ranging from 4 to 28, on the mechanical properties of polycrystalline B_6N_6, BC_3, BN, and C_3N_4 nanosheets is first studied. For each sample, simulation runs perform loading in one direction, and the stress–strain curves result for the corresponding directions. In the simulations, the temperature remains controlled around 300 K and the applied strain rate is 2.5×10^8 s^{-1}. The simulated stress–strain curves of PCSs under uniaxial tension provide the Young's modulus and tensile strength. Fig. 2 demonstrates the mechanical properties, including Young's modulus and tensile strength, with respect to the number of grains for polycrystalline B_6N_6, BC_3, BN, and C_3N_4 nanosheets. The results show that as the number of grains in the polycrystalline structure increases, the tensile strength decreases (Fig. 2(a)), which aligns with previous research [19,32]. For example, the tensile strength of polycrystalline BN, B_6N_6, BC_3, and C_3N_4 nanosheets with 4 grains is 88.82, 86.69, 58.71, and 48.68 GPa, respectively. This strength decreases to 75.70, 69.67, 49.09, and 39.89 GPa when the grain count increases to 24 grains. Additionally, as shown in Fig. 2(b), the Young's modulus of polycrystalline BN, BC_3, C_3N4_4, and B_6N_6 decreases until the number of grains reaches 24. This reduction arises from the increased density of grain boundaries and triple junctions as the grain count rises. At the atomic level, grain boundaries contain undercoordinated atoms, distorted bond angles, and residual strains. These structural imperfections act as stress concentrators, where the local stress can exceed the nominal applied stress. Consequently, inelastic deformation (bond stretching, rotation, and eventual breakage) initiates at boundaries at lower external loads compared to the pristine lattice. Furthermore, grain boundaries facilitate premature void nucleation and coalescence, bypassing the higher strength pathways of perfect crystalline regions.

Furthermore, the magnitude of strength reduction varies across materials, revealing distinct atomic-scale mechanisms. BN exhibits the smallest relative decrease (~15%), attributed to its relatively low-energy grain boundaries with minimal bond length distortion and the partial ionic character of B–N bonds, which resists boundary sliding. B_6N_6 (20% decrease) shows a larger reduction because its octahedral ring topology creates more distorted grain boundary geometries that reorient under stress, lowering the load-bearing capacity. BC_3 (16% decrease) experiences an intermediate reduction; however, its absolute strength remains lower than BN and B_6N_6 due to intrinsically weaker B–C bonds at the boundaries. C_3N_4 exhibits the largest reduction (~18% from 4 to 24 grains) and the lowest absolute strength. This is because the large 12-membered rings in C_3N_4 produce grain boundaries with a high density of undercoordinated nitrogen and carbon dangling bonds, which act as weak links that fail at significantly lower stresses.

Beyond 24 grains, the Young's modulus remains nearly constant for all four materials at 356.30 GPa (BN), 343.76 GPa (BC_3), 254.98 GPa (C_3N_4), and 245.15 GPa (B_6N_6). Mortazavi and Cuniberti [18] reported that for polycrystalline BN nanosheets, the elastic modulus decreases gradually with grain refinement but approaches a plateau when grain sizes fall below approximately 5 nm, beyond which further grain refinement yields negligible changes in stiffness. This

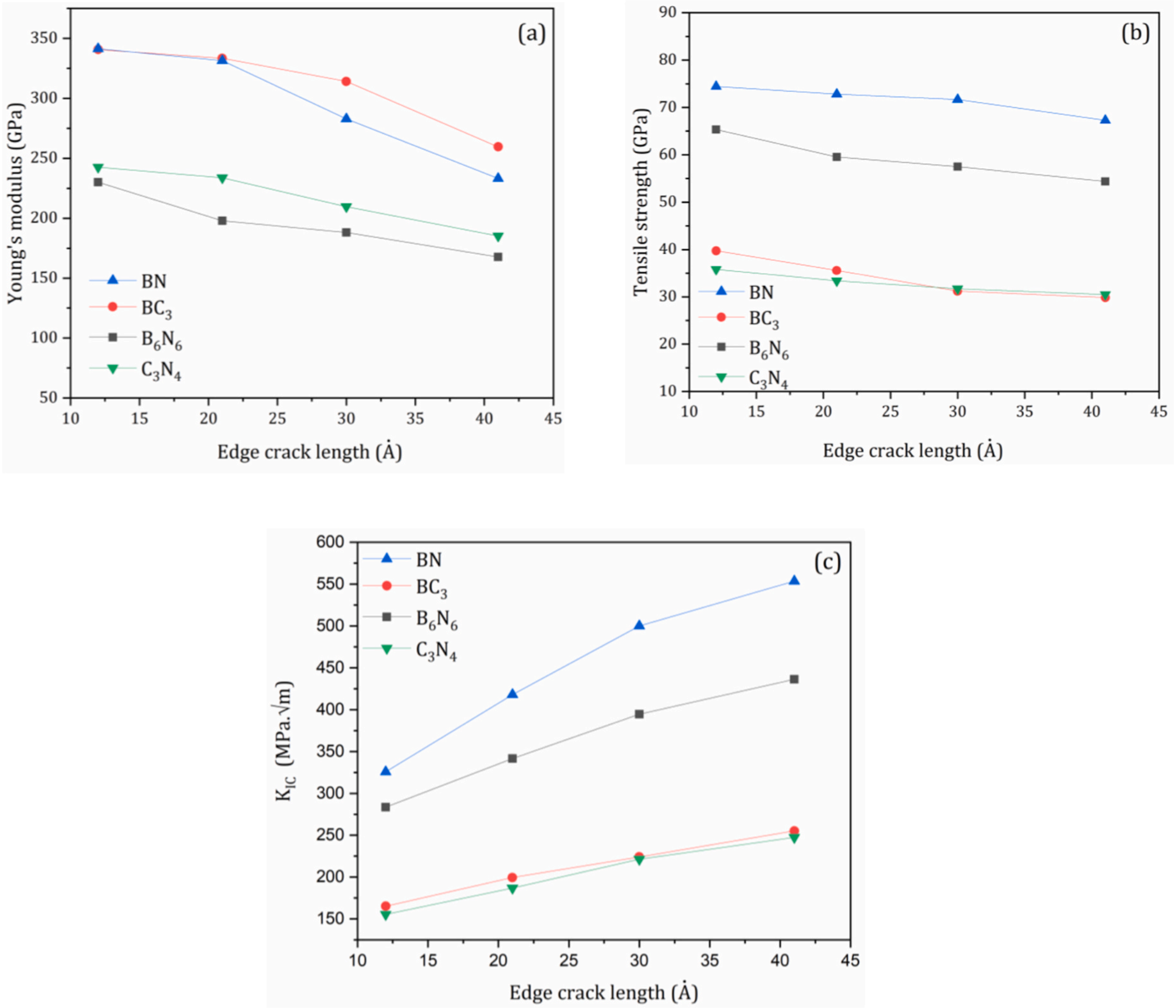

Fig. 6. (a) Young's modulus, (b) tensile strength, and (c) critical fracture toughness of the polycrystalline nanosheets as a function of edge crack lengths.

plateau indicates that beyond a critical grain boundary density, the mechanical response becomes dominated by boundary deformation mechanisms rather than by the pristine lattice. The saturation occurs because further grain refinement does not introduce new atomic-scale deformation modes; instead, the material behaves as a continuous nanocrystalline phase with stable effective properties.

The stress–strain curves of PCSs with 24 grains (Figs. 2(a) and 3) show that the tensile strength of the PCSs follows the trend: $C_3N_4<BC_3<B_6N_6<BN$. Furthermore, among the PCS samples, B_6N_6 exhibits the lowest Young's modulus, followed by C_3N_4 and BC_3, while BN shows the highest modulus (Fig. 2(b)). In order to better understand the fracture process, the ruptured configurations of polycrystalline B_6N_6, BC_3, BN, and C_3N_4 nanosheets with 24 grains under failure strain are also illustrated in Fig. 4. By comparing the failure strain among the polycrystalline B_6N_6, BC_3, BN, and C_3N_4 nanosheets, it is evident that polycrystalline B_6N_6, followed by BN, has the highest failure strain among the PCSs. It can also be seen that polycrystalline BC_3 and C_3N_4 have almost identical failure strain. Furthermore, as can be seen in Figs. 3 and 4, the tensile strength follows the trend of BN (76.76 GPa) > B_6N_6 (68.75 GPa) > BC_3 (55.59 GPa) > C_3N_4 (45.00 GPa). Moreover, integration and analysis of the stress–strain curve (see Fig. 3) reveal a clear toughness hierarchy among the investigated PCS samples: B_6N_6 (15.9 J/m^3) demonstrates the highest fracture energy, followed by BN (14.5 J/m3), BC_3 (5.7 J/m3), and C_3N_4 (5.1 J/m3). This ranking is consistent with their respective energy absorption capacities before fracture. It should be noted that the trend in fracture energy largely reflects the trend in failure strain.

The observation that polycrystalline B_6N_6 exhibits a lower Young's modulus (245.15 GPa vs. 356.30 GPa for BN at 24 grains) but higher fracture energy (15.9 vs. 14.5 J/m^3) arises from its distinct octahedral ring topology. In BN, the hexagonal honeycomb lattice provides a continuous load-bearing network with minimal structural redundancy [33]. Each B–N bond operates near its optimal stretching mode, resulting in high stiffness. In contrast, B_6N_6 contains octahedral structural units that act as internal hinges. Under tensile loading, these octahedra undergo localized reorientation and non-affine deformation before bond breaking occurs. This reorientation redistributes local stresses away from highly strained regions, delaying catastrophic failure and thereby increasing energy absorption (toughness). However, the same reorientation mechanism reduces the overall resistance to elastic deformation, manifesting as a lower Young's modulus. This trade-off between stiffness and toughness is a classic example of the stiffness-toughness paradox observed in many nanostructured materials. Lower modulus in BC_3 (343.76 GPa at 24 grains) compared to BN (356.30 GPa) originates from (i) intrinsically weaker/longer B–C bonds (~1.55 Å vs. 1.45 Å for B–N in BN [33]), (ii) hybridization mismatch between B (sp^2-like) and C (sp^2 graphitic) creating localized pre-strains, and (iii) compliant graphitic domains at grain boundaries. The low fracture energy of BC_3 (5.7 J/m^3) arises because C-rich grain boundaries form weak links that propagate cracks without energy dissipation mechanisms like bond rotation or crack bridging [34]. C_3N_4 exhibits the lowest Young's modulus among all four compositions (254.98 GPa at 24 grains), which

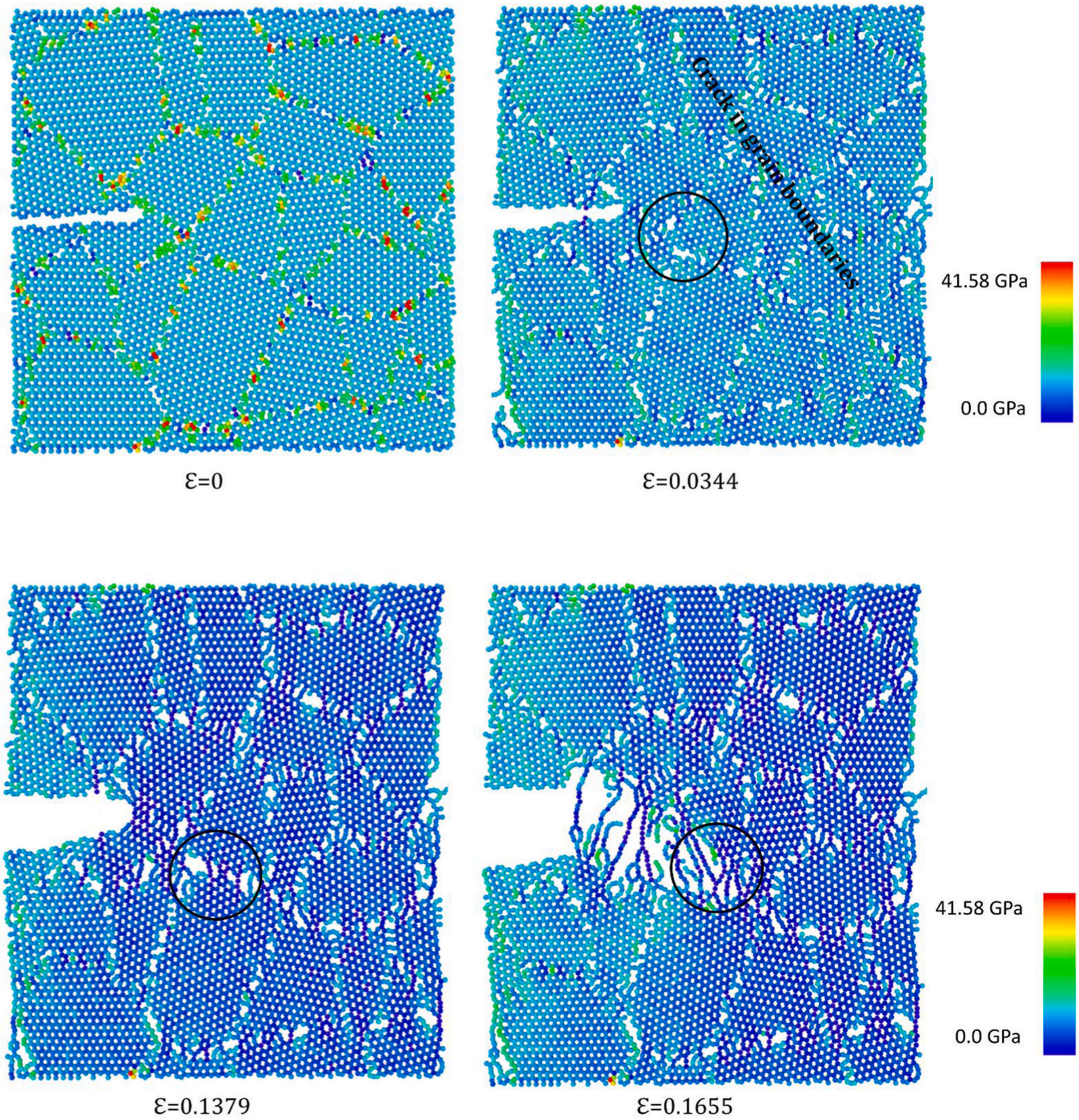

Fig. 7. Failure process in a polycrystalline BC_3 nanosheet with an edge pre-crack length of 40 Å.

is attributed to (i) absence of boron, (ii) larger ring sizes (12-membered rings) reducing bond areal density, and (iii) undercoordinated N and C dangling bonds at grain boundaries. The lowest fracture energy of C_3N_4 (5.1 J/m^3) stems from brittle intergranular failure: highly directional C–N bonds at triple junctions cannot undergo plastic deformation, leading to rapid crack propagation with minimal energy absorption [34,35].

Consequently, the combined analysis of Young's modulus, tensile strength, failure stress, and toughness demonstrates that polycrystalline BN nanosheets exhibit superior mechanical performance among all tested materials, outperforming B_6N_6, BC_3, and C_3N_4 in Young's modulus (356.30 vs. 245.15-343.76 GPa at 24 grains), tensile strength (75.70, vs. 39.89-69.67 GPa at 24 grains), failure stress (76.76 vs. 45.00-68.75 GPa) and fracture energy (14.5 vs. 5.1–15.9 J/m^3 at 24 grains). This consistent superiority highlights BN's structural advantages for applications requiring both high stiffness and strength, whereas B_6N_6 may be preferable when fracture energy (damage tolerance) is the primary design criterion.

The effect of temperature on the mechanical properties of PCSs with 24 grains is examined. Fig. 5 shows the variations in Young's modulus and tensile strength with respect to temperature for polycrystalline BN, BC_3, C_3N_4, and B_6N_6 nanosheets. As shown in Fig. 5(a) the Young's modulus of BN, BC_3, C_3N_4, and B_6N_6 lies in the range of 360.1–307.7, 345.3-230.3, 257.2-203.4 and 246.8-185.6 GPa, respectively. Furthermore, the tensile strength of BN, B_6N_6, BC_3, and C_3N_4 falls in the range of 96.1-40.0, 90.6-14.3, 53.6-20.2, and 47.7-13.1 GPa, respectively (Fig. 5 (b)). The calculated percentage decrease in Young's modulus and tensile strength from 100 to 1500 K for BN, B_6N_6, BC_3, and C_3N_4 are (15% and 58%), (25% and 84%), (33% and 62%), and (21% and 72%), respectively. Consequently, the percentage reduction in Young's modulus follows the trend $BC_3 > B_6N_6 > C_3N_4 >$ BN, while for tensile strength, the trend is $B_6N_6 > C_3N_4 > BC_3 >$ BN. The greater thermal sensitivity of tensile strength versus modulus arises because strength follows an Arrhenius dependence (activation energy), whereas modulus scales linearly with temperature via anharmonicity [36,37]. BN shows the highest thermal stability due to its high optical phonon frequency (E_{2g} ~1370 cm^{-1}), low anharmonicity (γ ~1.5), and absence of low-frequency soft modes [36]. BC_3 exhibits the largest modulus

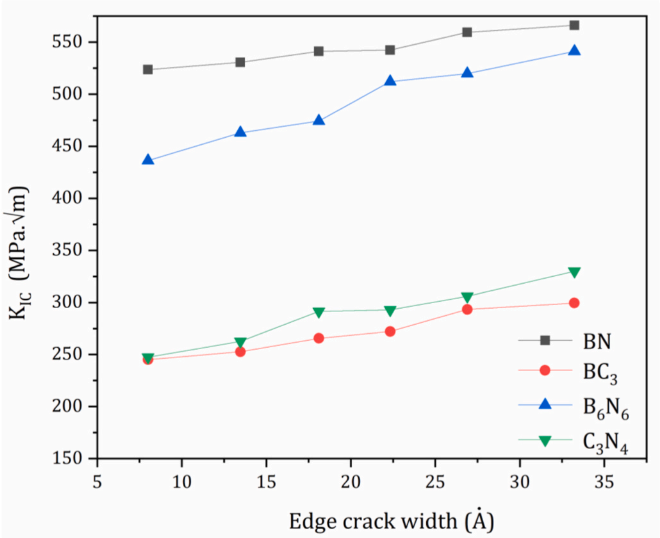

Fig. 8. The critical fracture toughness versus edge crack width for polycrystalline nanosheets with the edge crack length of 40 Å

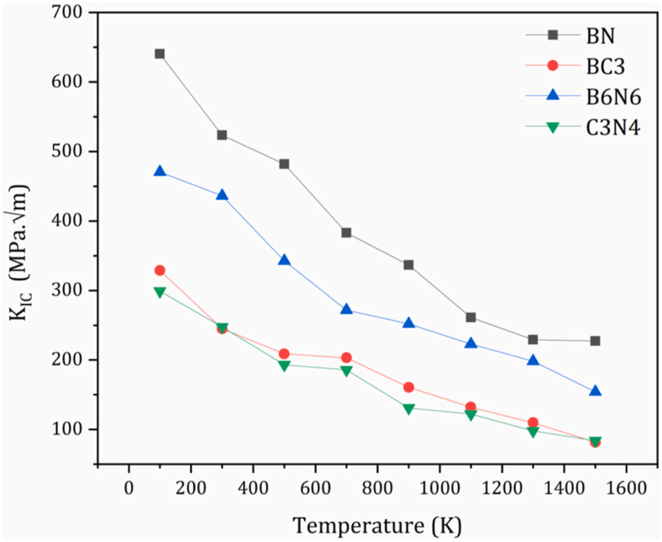

Fig. 9. The critical fracture toughness of pre-cracked polycrystalline nanosheets with an edge pre-cracks length of 40 Å and width of 7.8 Å versus temperature.

reduction (33%), attributed to its lower B–C phonon frequency (~1050 cm^{-1}), higher anharmonicity (γ ~2.2), and graphitic flexural modes (<500 cm^{-1}) [37]. B_6N_6 shows the largest strength reduction (84%) because its octahedral rings introduce low-frequency torsional modes (~200–400 cm^{-1}) that thermally activate non-affine reorientations, promoting premature bond breaking [38]. C_3N_4 displays intermediate sensitivity; its 12-membered rings create breathing modes (~250–500 cm^{-1}) that couple with the tensile direction, reducing stiffness with temperature [37]. Thus, the thermal stability hierarchy (BN > C_3N_4 > BC_3 > B_6N_6 for strength) is governed by phonon frequencies, anharmonicity, and the presence of soft modes from non-hexagonal topologies.

The effect of edge pre-crack length on the mechanical properties of PCSs (24 grains) is investigated in this section at room temperature. The selected edge crack lengths (12, 20, 30, and 40 Å) correspond to approximately 8–27% of the nanosheet length (150 Å), ensuring that finite-size effects are minimized while covering the experimentally relevant defect size range for polycrystalline 2D materials. Cracks smaller than 12 Å behave similarly to intrinsic grain boundary defects already present in our polycrystalline structures (as shown in Fig. 4), while cracks larger than 40 Å would exceed half the sheet width and introduce artificial boundary effects. Fig. 6 illustrates the computed Young's modulus, tensile strength, and critical fracture toughness (K_{IC}) different edge crack lengths, including 12, 20, 30, and 40 Å. The K_{IC} is calculated using Equation (1):

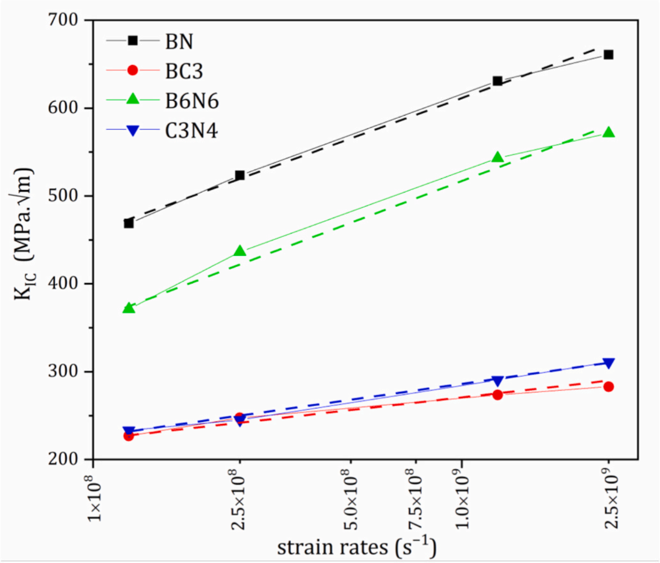

Fig. 10. The effect of strain rate on the critical fracture toughness of the polycrystalline nanosheets with an edge pre-crack (length = 40 Å and width = 7.8 Å).

$$K_{IC} = \sigma_f \sqrt{\pi a} \tag{1}$$

where σ_f denotes the failure stress and a is the pre-crack length. Notably, the fracture surface is perpendicular to the tensile direction. It should be noted that the application of Eq. (1) to PCSs requires careful consideration. In classical linear elastic fracture mechanics (LEFM), the stress field near a sharp crack tip follows a singular $1/\sqrt{r}$ distribution. However, in polycrystalline materials, grain boundaries located near the crack tip can disturb this singular field by redistributing stress or causing local inelastic deformation. In the present study, to minimize such effects, all pre-cracks were introduced within single crystalline grains and placed away from grain boundaries and triple junctions. Fig. 6 shows that increasing the length of the pre-crack leads to a decrease in both the Young's modulus (Fig. 6(a)) and tensile strength (Fig. 6(b)) of the PCSs. Conversely, the critical fracture toughness (Fig. 6(c)) is observed to increase. It can also be found that the critical fracture toughness of materials increases linearly with increasing pre-cracking length. The slope of this increase is highest for polycrystalline BN with a value of 6.93 MPa/ $\sqrt{m}$, followed by B_6N_6 with a value of 5.28 MPa/ $\sqrt{m}$, C_3N_4 with a value of 3.20 MPa/ $\sqrt{m}$, and finally BC_3 with a value of 2.64 MPa/ $\sqrt{m}$.

In LEFM, the critical stress intensity factor K_{IC} is defined as a material constant and should be independent of crack length. The observed linear increase of K_{IC} with pre-crack length (Fig. 6(c)) clearly indicates that LEFM is not strictly applicable to our PCSs at the atomistic scale. This deviation is expected due to the inherent heterogeneity of grain boundaries, the finite nanoscale dimensions of the system, and the possibility of a non-singular stress field at the crack tip. Therefore, the K_IC values reported here should be interpreted as apparent fracture toughness used for comparative purposes across the four materials under identical simulation conditions. The relative ranking and trends (e.g., sensitivity to crack length, temperature, and strain rate) are reliable, but absolute values should not be directly compared with continuum LEFM

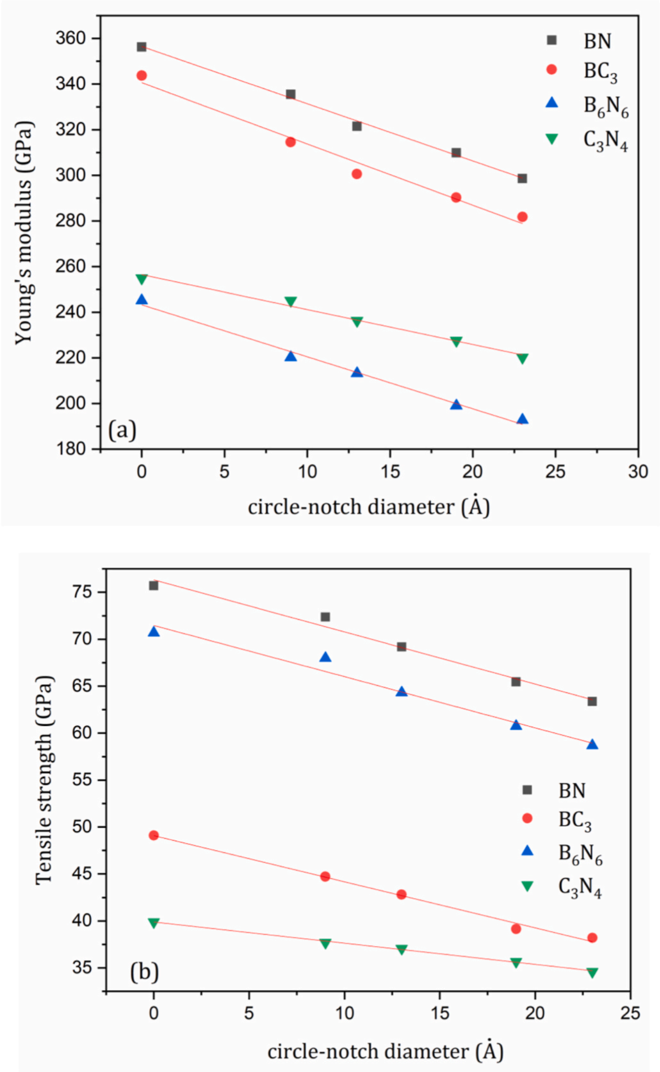

Fig. 11. The mechanical characteristics of polycrystalline B_6N_6, BC_3, BN, and C_3N_4 with different circular-notch diameters.

predictions. According to the critical fracture toughness diagram in Fig. 6(c), the critical fracture toughness of BN is higher than the other samples. Furthermore, BC_3 and C_3N_4 have nearly identical critical fracture toughness, both showing the lowest values. Hence, the results show that despite the high mechanical properties of BN compared to the other tested PCSs, it exhibits greater sensitivity to crack propagation. Conversely, BC_3 and C_3N_4 demonstrate the lowest crack sensitivity. A direct comparison between the two fracture resistance metrics used in this study reveals an apparent but instructive reversal. The first metric is the fracture energy obtained from integrating the area under the stress-strain curve, where B_6N_6 exhibits a higher value (15.9 J/m^3) compared to BN (14.5 J/m^3). The second metric is the critical fracture toughness, $K_{IC} = \sigma_f \sqrt{\pi a}$ from Eq. (1), where Fig. 6(c) shows that BN exhibits a higher K_{IC} than B_6N_6. This apparent reversal is not a contradiction but rather an important physical insight. In B_6N_6, the octahedral ring topology enables significant nonlinear deformation and bond reorientation before failure, which absorbs substantial energy (giving higher fracture energy) but does not proportionally increase the stress concentration at the crack tip (giving lower K_{IC}). In contrast, BN with its stable hexagonal honeycomb lattice and strong B-N bonds behaves in a more linear elastic manner up to failure, resulting in higher crack tip stress concentration (higher K_{IC}) but less pre-failure energy absorption (lower fracture energy). Consequently, these two metrics provide complementary information: B_6N_6 is preferred for applications requiring high energy absorption (e.g., impact resistance), while BN is superior for applications where resistance to crack propagation from existing defects is critical (e.g., defect-tolerant structural designs). In crack-insensitive fractures, such as those observed in polycrystalline BC_3 and C_3N_4, failure occurs independently of the crack tip, behaving similarly to that of a crack-free sheet. As a result, despite the presence of a stress concentration region at the crack tip, the maximum atomic stress at the crack tip is much lower than that at grain boundaries and triple junctions. Therefore, in polycrystalline BC_3 and C_3N_4, grain boundaries and triple junctions are energetically more favorable sites for rupture. Fig. 7 for polycrystalline BC_3 supports this reasoning.

To investigate the influence of the crack tip on the critical fracture toughness of PCSs, edge pre-cracked polycrystalline BN, B_6N_6, C_3N_4, and BC_3 were also used, each with varying crack widths. The crack width varied from 7.8 to 33.2 Å while the crack length was kept at 40 Å. As shown in Fig. 8, critical fracture toughness increases with increasing crack width because the local stress concentration at the crack tip is reduced [39]. Moreover, the percentage of this decrease is in the order of $C_3N_4 > BC_3 > B_6N_6 > BN$, which is also due to the lower crack sensitivity in C_3N_4 and higher crack sensitivity in BN compared to the other samples.

Temperature and strain rate play important roles in the mechanical properties of nanomaterials measured in tensile tests. The influence of temperature on the critical fracture toughness of polycrystalline B_6N_6, BC_3, BN, and C_3N_4 nanosheets was first investigated. This involved using edge pre-cracks with a length of 40 Å (width = 7.8 Å) across a temperature range of 100 to 1500 K. The calculated critical fracture toughness of samples versus temperature is shown in Fig. 9. As expected, the critical fracture toughness of pre-cracked PCSs, decrease with the increasing temperature. The results show that the percentage reduction in critical fracture toughness with increasing temperature is greatest for polycrystalline BC_3 and lowest for polycrystalline BN. The critical fracture toughness of polycrystalline BN, B_6N_6, C_3N_4 and BC_3 show reduction 64%, 67%, 72%, and 75%, respectively. Therefore, the sensitivity to crack decreases with increasing temperature, and as expected, this decreases in crack-sensitivity is greater in BC_3 than in the other samples. It can also be found that the temperature sensitivity in pre-cracked PCSs follows the order: $BC_3 > C_3N_4 > B_6N_6 > BN$.

The effect of strain rate on the mechanical properties of the PCSs with an edge pre-crack (length = 40 Å and width = 7.8 Å), is examined in this study by applying strain rates in the range of 2.5×10^6–2.5×10^9 s^{-1}. The critical fracture toughness was obtained from the simulated stress–strain curves and are plotted in Fig. 10 as a function of strain rate. An increase in strain rate leads to a corresponding increase in critical fracture toughness. This behavior can be explained by the limited opportunity for atomic rearrangement during tensile deformation, which increases the likelihood of bond breaking and causes the material to behave more brittle at high strain rates. Furthermore, by increasing the strain rate may prevent the growth of fine cracks due to insufficient time for crack propagation. Fig. 11 also reveals a linear relationship between the critical fracture toughness and the logarithm of the strain rate, a finding consistent with previous literature [40–42]. The slope of these lines for BN, B_6N_6, C_3N_4 and BC_3 are equal to 143, 141, 66 and 41 MPa $\sqrt{m}$, respectively. Therefore, pre-cracked PCSs are sensitive to the strain rate and follows the trend $BC_3 < C_3N_4 < B_6N_6 < BN$.

This section considers the effect of circular notch-shaped defects on the mechanical properties of PCSs. Six circular notch diameters, ranging from 9 to 23 Å, were examined. The mechanical characteristics of polycrystalline B_6N_6, BC_3, BN, and C_3N_4 having different notch diameters are compared in Fig. 11. As shown in the figure, both the calculated Young's modulus and tensile strength decrease with increasing circle-notch diameter. Moreover, the mechanical properties maintain an approximately linear relationship with the circular notch diameter. As can be seen in Fig. 11, the slope of the change in Young's modulus and tensile strength for polycrystalline B_6N_6, BC_3, BN, and

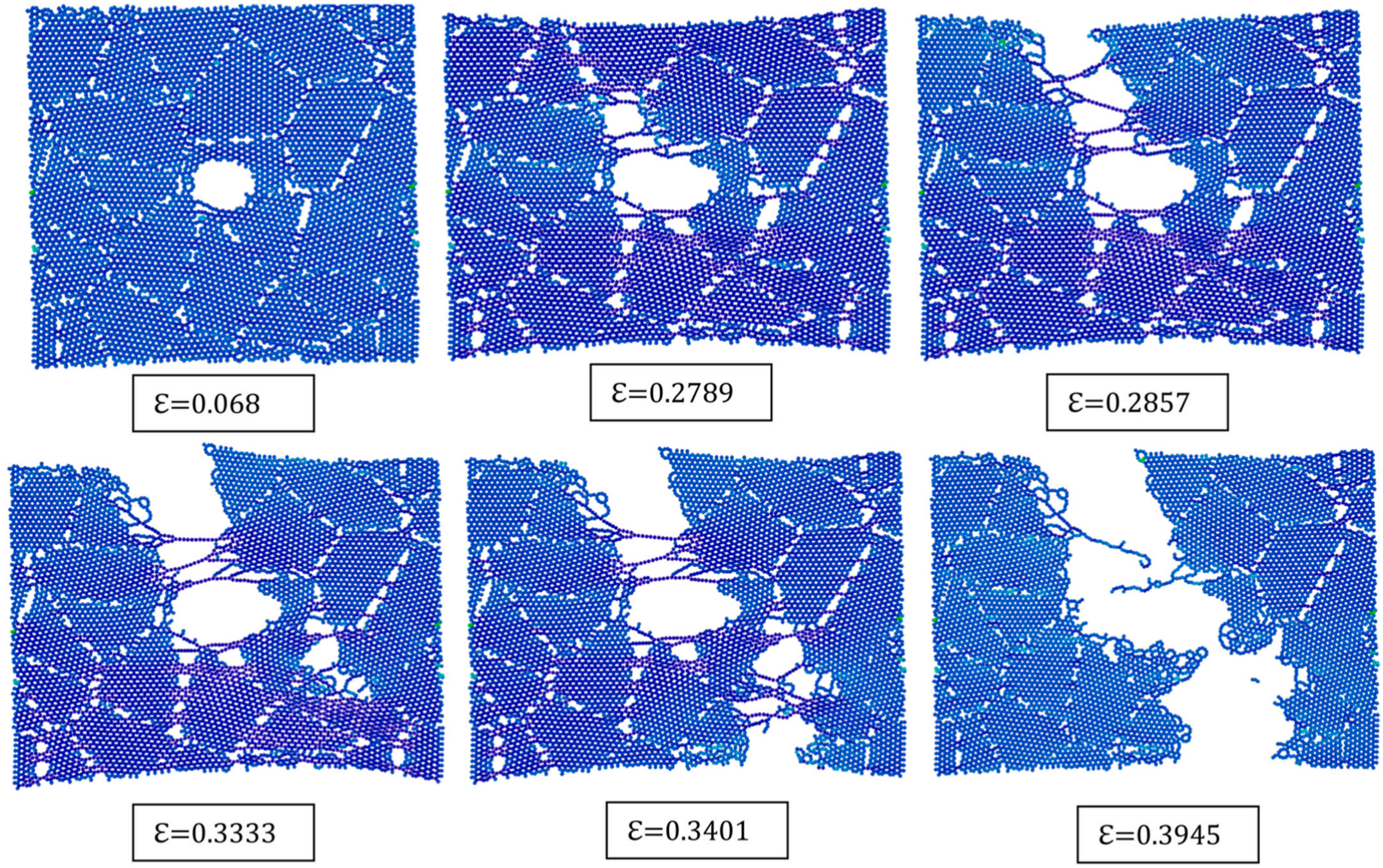

Fig. 12. Failure process into a polycrystalline BN nanosheet exposed to a circular-notch shaped defects with the notch diameter of 23 Å.

C_3N_4 nanosheets follows the order $C_3N_4 < BC_3 < B_6N_6 < BN$.

To investigate the failure patterns of the polycrystalline materials, the failure process for a polycrystalline BN sample exposed to a circular notch-shaped defect is illustrated in Fig. 12. As illustrated in this figure, the fracture is initiated at the notch, a region of high stress concentration, and the ensuing crack propagates radially from the notch in a direction perpendicular to the applied tensile load, culminating in the complete rupture of the polycrystalline structure. Beyond this, according to Fig. 13, the crack growth rate in the polycrystalline BC_3 sample is higher than in all other samples, followed by the C_3N_4, B_6N_6, and BN samples. Consequently, polycrystalline BN is more sensitive and polycrystalline C_3N_4 is less sensitive to circular defect than the other samples.

This section investigates the mechanical properties of polycrystalline B_6N_6, BC_3, BN, and C_3N_4 nanotubes with a random grain number of 24. Uniaxial tensile tests were performed on nanotubes with a constant length of 50 Å and diameters ranging from 12.7 to 31.8 Å. The mechanical properties including Young's modulus, tensile strength and failure strain of PCNs are listed in Fig. 14. It is evident that the Young's modulus increases, while the tensile strength and failure strain decreases with increasing diameter of the nanotubes. These results show that the toughness of PCNs decreases with increasing diameter, regardless of the type of nanotube. It is also apparent that the rate of change in Young's modulus, tensile strength and failure strain for nanotubes follows the trend of $C_3N_4 > BN > BC_3 > B_6N_6$. For instance, the percentage change of Young's modulus, tensile strength and failure strain of polycrystalline C_3N_4 nanotubes are equal to 49%, 41% and 49% while in polycrystalline B_6N_6 nanotubes are equal to 21%, 10% and 29%, respectively. Furthermore, Fig. 15 presents a snapshot of the failure process in polycrystalline B_6N_6nanotubes. The results confirm that with increasing nanotube diameter, the nanotubes become more brittle and crack growth becomes faster.

In terms of the temperature effect, it was found that the mechanical properties of PCNs with a diameter of 12.7 Å generally decreased with increasing temperature, consistent with previously obtained results, as presented in Fig. 16. According to this figure, a comparison is made between the Young's modulus of polycrystalline C_3N_4, BN, BC_3, and B_6N_6 nanotubes. This figure clearly shows that, increasing temperature leads to 70%, 45%, 42%, and 34% changes in the modulus of polycrystalline C_3N_4, BN, BC_3, B_6N_6 nanotubes, respectively. Thus, polycrystalline C_3N_4 nanotube is the most sensitive to temperature among other nanotubes, followed by BN, BC_3, B_6N_6, respectively.

Despite the comprehensive insights provided by the present study, several important avenues remain open for future investigation. First, the effects of intragranular vacancies and point defects (e.g., single and double vacancies, Stone–Wales defects) on the mechanical response of polycrystalline B–C–N nanosheets should be systematically examined, particularly in combination with grain boundaries. Second, the influence of grain size distribution (rather than average grain size or grain count) and grain boundary morphology (e.g., tilt vs. twist boundaries) on fracture toughness and crack path selection warrants further attention. Third, extending the present analysis to multilayer PCSs and heterostructures (e.g., BN/C_3N_4 or BC_3/graphene interfaces) would better capture the behavior of realistic device architectures. Fourth, machine learning interatomic potentials (such as neural network potentials or Gaussian approximation potentials) could be developed for B–C–N systems to enable larger-scale and longer-time simulations beyond the current Tersoff potential. Finally, experimental validation of the predicted trends in fracture toughness and crack sensitivity (e.g., via in-situ TEM nanomechanical testing) would be highly valuable to confirm the atomistic insights reported here.

This study is based solely on MD simulations using the Tersoff

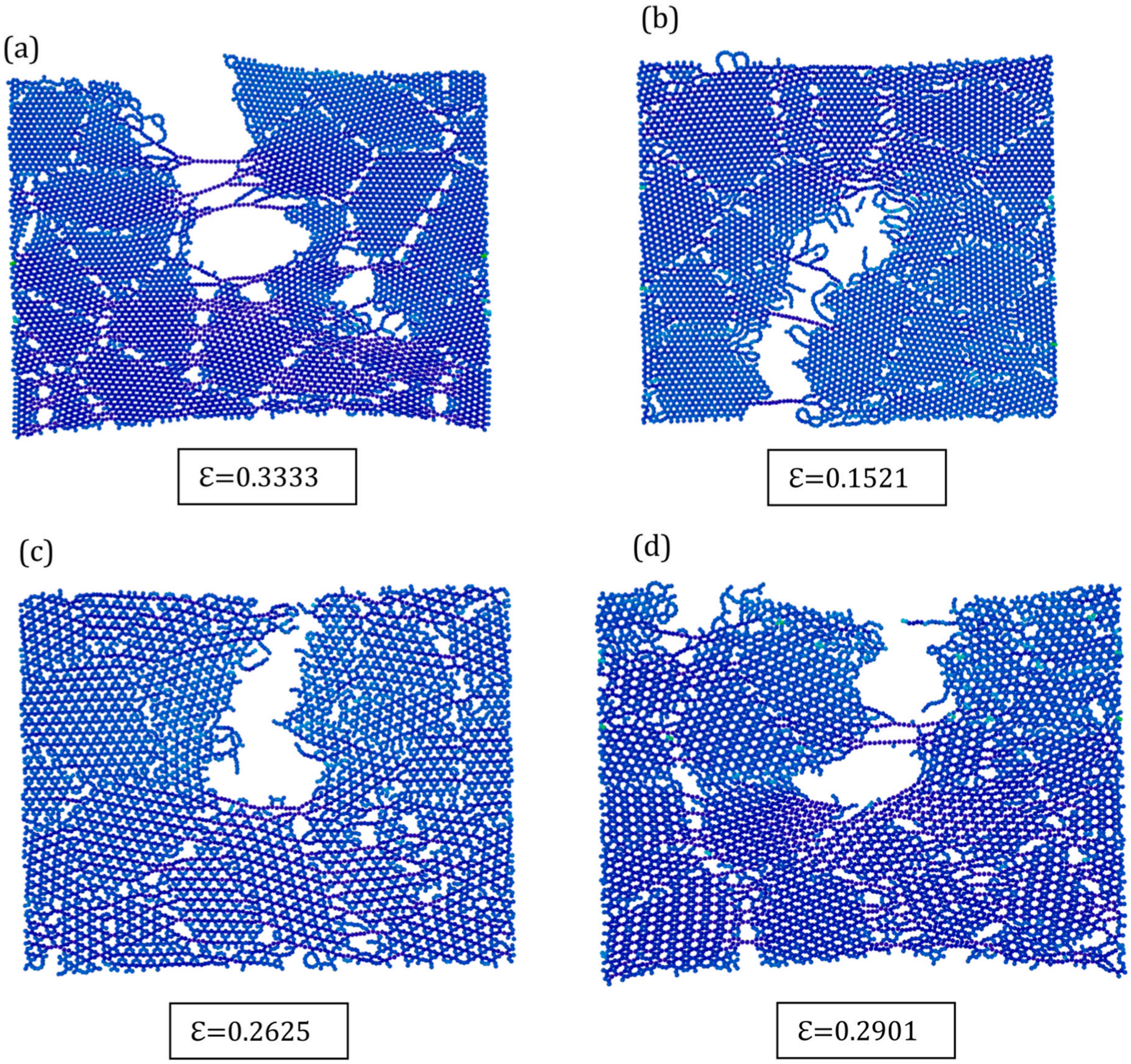

Fig. 13. crack growth rate snapshots in a) BN, b) BC_3, c) B_6N_6 and d) C_3N_4 polycrystalline nanosheet.

potential, and direct experimental validation is currently lacking. The polycrystalline models are idealized (Voronoi tessellation with random grain orientations), whereas real microstructures typically include grain size distributions, diverse boundary types, and intragranular defects. The simulated strain rates (10^6–10^9 s^{-1}) are considerably higher than experimental rates (10^{-4}–10^{-2} s^{-1}), a common limitation of atomistic simulations. Wall thickness assumptions affect absolute modulus values, although relative comparisons between materials remain reliable. Finally, only single-layer nanosheets and nanotubes are considered; multilayer structures, heterostructures, and substrate effects are not addressed. These limitations should be taken into account when extrapolating the results to experimental or real-world applications.

4. Conclusion

MD simulations reveal that the mechanical properties, fracture toughness, and crack-propagation behavior of polycrystalline B_6N_6, BN, BC_3, and C_3N_4 nanosheets and nanotubes are strongly influenced by the number of grains, temperature, strain rate, and structural defects. BN nanosheets exhibit the highest Young's modulus, tensile strength, and thermal stability, while B_6N_6 shows the greatest fracture toughness. Analyses of pre-cracks and circular notches indicate that BN is most sensitive to crack propagation, whereas BC_3 and C_3N_4 display crack-insensitive fracture behavior, with failure frequently initiating at grain boundaries rather than crack tips. Increasing strain rate enhances fracture toughness by limiting atomic rearrangement and crack growth. For nanotubes, larger diameters increase stiffness but reduce tensile strength, failure strain, and fracture toughness, with C_3N_4 nanotubes showing the highest temperature sensitivity.

CRediT authorship contribution statement

Morteza Ghorbanzadeh Ahangari: Conceptualization, Data curation, Methodology, Software, Supervision, Writing – original draft, Writing – review & editing. **Mostafa Fathalian:** Formal analysis, Visualization, Writing – review & editing. **Sajjad Dargahi:** Data curation, Formal analysis, Software, Writing – original draft.

Declaration of competing interest

The authors declare that they have no known competing financial interests or personal relationships that could have appeared to influence the work reported in this paper.

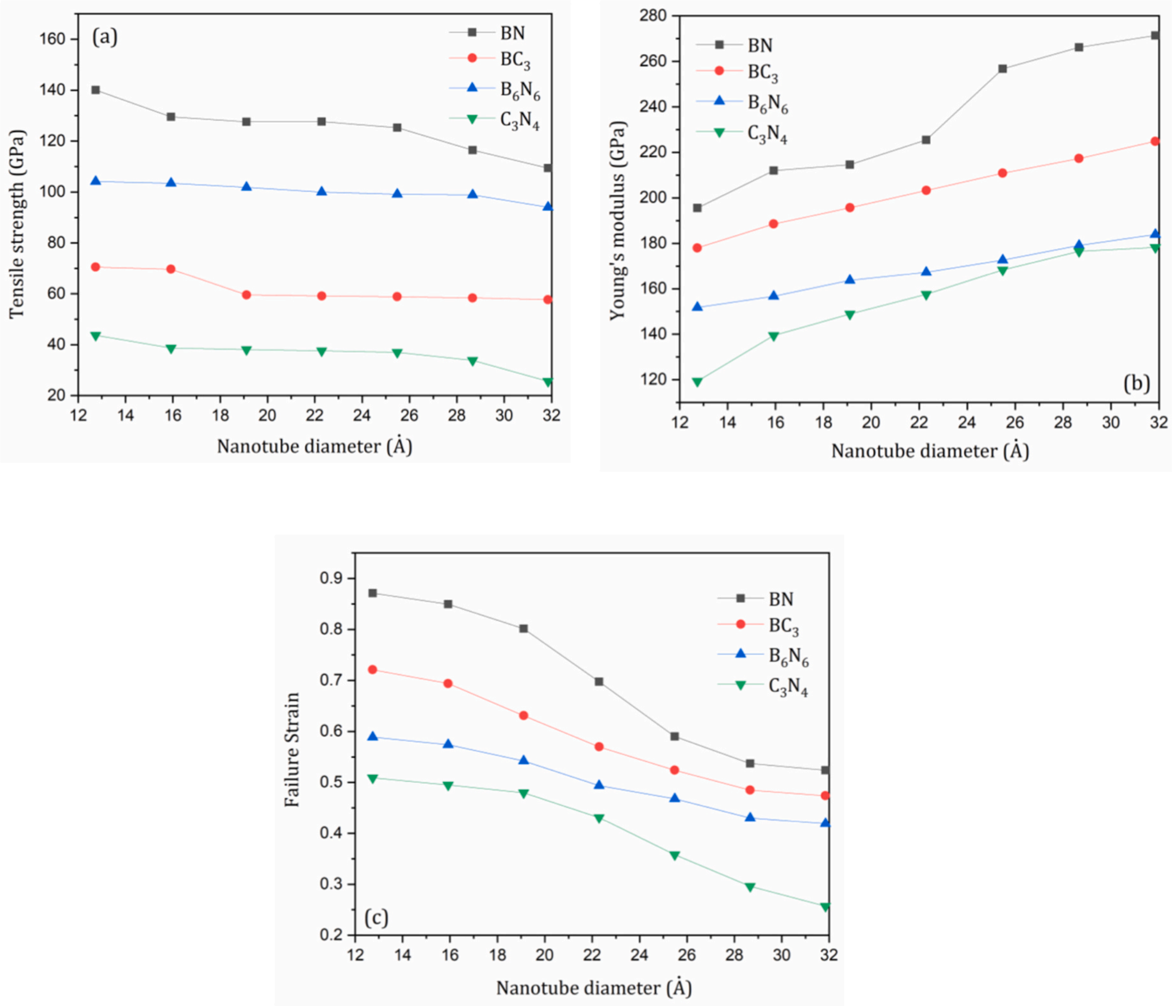

Fig. 14. The mechanical properties include of (a) Young's modulus, (b) tensile strength and (c) failure strain of polycrystalline nanotubes.

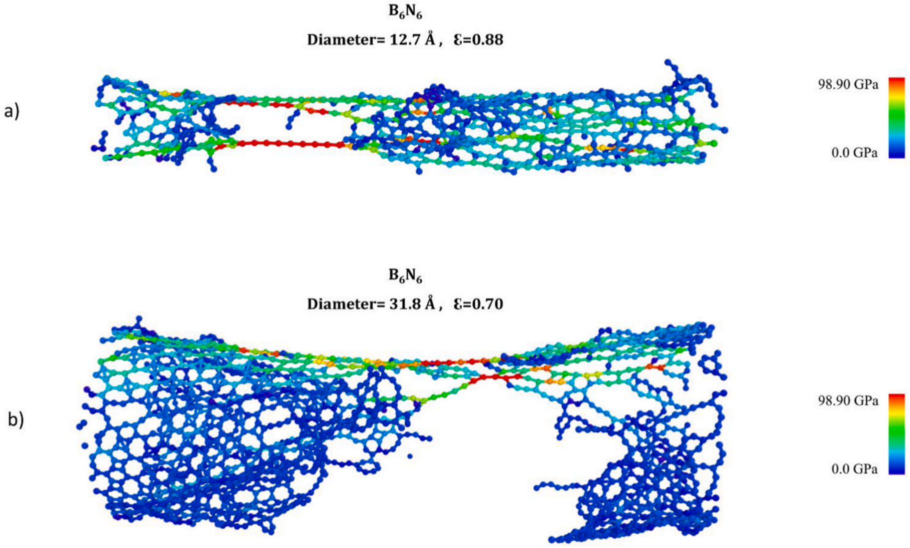

B_6N_6
Diameter= 12.7 Å , Ɛ=0.88

B_6N_6
Diameter= 31.8 Å , Ɛ=0.70

Fig. 15. The snapshot of the failure process in polycrystalline B_6N_6 nanotubes with the diameter of a) 12.7 Å and b) 31.8 Å.

Data availability

Data will be made available on request.

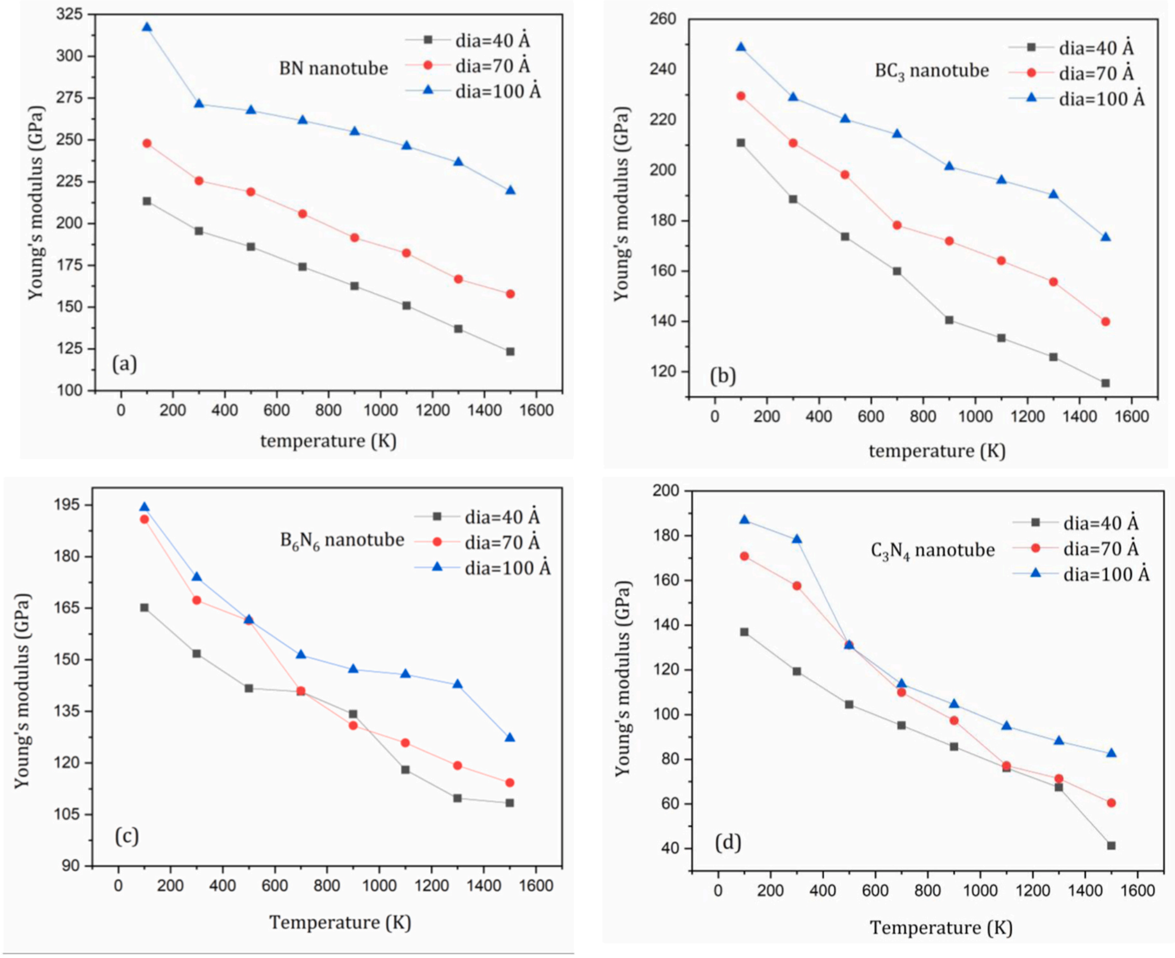

Fig. 16. Mechanical properties of polycrystalline nanotubes with diameter of 12.7 Å as a function of temperature.

References

[1] Li, J., Yang, X., Zhang, Z., Yang, W., Duan, X., Duan, X., 2024. Towards the scalable synthesis of two-dimensional heterostructures and superlattices beyond exfoliation and restacking. Nat. Mater. 23, 1326–1338. https://doi.org/10.1038/s41563-024-01989-8.

[2] Wang, G., Hou, H., Yan, Y., Jagatramka, R., Shirsalimian, A., Wang, Y., et al., 2023. Recent advances in the mechanics of 2D materials. Int. J. Extrem. Manuf. 5, 032002. https://doi.org/10.1088/2631-7990/accda2.

[3] Chen, J., Mohammed, A.A., Fadhil, D.A., Al-Bahrani, M., Salahshour, S., Sabetvand, R., 2024. The effect of constant electric field on the crack growth process of aluminum nanosheet using molecular dynamics simulation. J. Mol. Graph. Model. 132, 108841. https://doi.org/10.1016/j.jmgm.2024.108841.

[4] Singh, S.K., Chaurasia, A., Verma, A., 2023. Basics of density functional theory, molecular dynamics, and monte carlo simulation techniques in materials science. In: Verma, A., Sethi, S.K., Ogata, S. (Eds.), Coating Materials: Computational Aspects, Applications and Challenges. Springer Nature, singapore, pp. 111–124.

[5] Chigo-Anota, E., Alejandro, M.A., Hernández, A.B., Torres, J.S., Castro, M., 2016. Long range corrected-wPBE based analysis of the H_2O adsorption on magnetic BC_3 nanosheets. RSC Adv. 6, 20409–20421. https://doi.org/10.1039/C5RA27231A.

[6] Yang, S., Li, W., Ye, C., Wang, G., Tian, H., Zhu, C., et al., 2017. C_3N—A 2D crystalline, hole-free, tunable-narrow-bandgap semiconductor with ferromagnetic properties. Adv. Mater. 29, 1605625. https://doi.org/10.1002/adma.201605625.

[7] Liu, J., Liu, Y., Liu, N., Han, Y., Zhang, X., Huang, H., et al., 2015. Metal-free efficient photocatalyst for stable visible water splitting via a two-electron pathway. Science 347, 970–974. https://doi.org/10.1126/science.aaa3145.

[8] Verma, A., Sharma, S., 2022. Atomistic simulations to study thermal effects and strain rate on mechanical and fracture properties of graphene like BC3. In: Verma, A., Rangappa, S.M., Ogata, S., Siengchin, S. (Eds.), Forcefields for atomistic-scale Simulations: Materials and Applications. Springer Nature, singapore, pp. 237–252.

[9] Ke, T., Shen, S., Yang, K., Lin, D., 2022. In situ fabrication of $Bi_2O_3/C_3N_4/TiO_2$@C photocatalysts for visible-light photodegradation of sulfamethoxazole in water. Appl. Surf. Sci. 580, 152302. https://doi.org/10.1016/j.apsusc.2021.152302.

[10] Gnanaguru, M.V.L., Ghangrekar, M.M., Chowdhury, S., 2024. 2D–2D g-C_3N_4/WS_2 Z-scheme heterojunction: comparison of the photocatalytic degradation of tetracycline and sulfamethoxazole. J. Photochem. Photobiol., A 456, 115818. https://doi.org/10.1016/j.jphotochem.2024.115818.

[11] Li, J., Sun, T., Deng, Y., Liu, H., Guan, R., Li, C., et al., 2025. Construction of photocatalytic-persulfate synergistic system for efficient removal of environmental pollutants. Sep. Purif. Technol. 360, 131033. https://doi.org/10.1016/j.seppur.2024.131033.

[12] Zhu, B., Zhang, L., Cheng, B., Yu, J., 2018. First-principle calculation study of tri-s-triazine-based g-C_3N_4: a review. Appl. Catal., B 224, 983–999. https://doi.org/10.1016/j.apcatb.2017.11.025.

[13] Mortazavi, B., 2017. Ultra high stiffness and thermal conductivity of graphene-like C_3N. Carbon 118, 25–34. https://doi.org/10.1016/j.carbon.2017.03.029.

[14] Su, T., Chao, R., Yu, T., Hu, S., Pan, H., Zhang, B., et al., 2026. Progress and perspectives of high-quality mechanical properties testing and mechanisms for 2D materials. Int. J. Extrem. Manuf. 8, 012002. https://doi.org/10.1088/2631-7990/ae0216.

[15] Yuan, X., Wang, Y., 2018. Radial deformation of single-walled carbon nanotubes adhered to solid substrates and variations of energy: atomistic simulations and continuum analysis. Int. J. Solid Struct. 144–145, 145–159. https://doi.org/10.1016/j.ijsolstr.2018.04.021.

[16] Fathalian, M., Darban, H., Postek, E., 2025. Atomistic insights into tensile damage of functionally Graded Al-SiC composites. Int. J. Mech. Sci. 288, 110012. https://doi.org/10.1016/j.ijmecsci.2025.110012.

[17] Fathalian, M., Postek, E., Tahani, M., Sadowski, T., 2024. Effect of diffusion on the ultimate axial load of complex-shaped Al-SiC samples: a molecular dynamics study. Molecules 29. https://doi.org/10.3390/molecules29143343.

[18] Mortazavi, B., Cuniberti, G., 2014. Mechanical properties of polycrystalline boron-nitride nanosheets. RSC Adv. 4, 19137–19143. https://doi.org/10.1039/C4RA01103A.

[19] Chen, M., Quek, S., Sha, Z., Chiu, C., Pei, Q., Zhang, Y., 2015. Effects of grain size, temperature and strain rate on the mechanical properties of polycrystalline graphene – a molecular dynamics study. Carbon 85, 135–146. https://doi.org/10.1016/j.carbon.2014.12.092.

[20] Elapolu, M.S., Tabarraei, A., 2021. Mechanical and fracture properties of polycrystalline graphene with hydrogenated grain boundaries. J. Phys. Chem. C 125, 11147–11158. https://doi.org/10.1021/acs.jpcc.1c01328.

[21] Ahangari, M.G., 2015. Effect of defect and temperature on the mechanical and electronic properties of graphdiyne: a theoretical study. Physica E 66, 140–147. https://doi.org/10.1016/j.physe.2014.10.016.

[22] Ahangari, M.G., Mashhadzadeh, A.H., Fathalian, M., Dadrasi, A., Rostamiyan, Y., Mallahi, A., 2019. Effect of various defects on mechanical and electronic properties of zinc-oxide graphene-like structure: a DFT study. Vacuum 165, 26–34. https://doi.org/10.1016/j.vacuum.2019.04.003.

[23] Shirazi, A., Abadi, R., Izadifar, M., Alajlan, N., Rabczuk, T., 2018. Mechanical responses of pristine and defective C_3N nanosheets studied by molecular dynamics simulations. Comput. Mater. Sci. 147, 316–321. https://doi.org/10.1016/j.commatsci.2018.01.058.

[24] Mortazavi, B., Shahrokhi, M., Raeisi, M., Zhuang, X., Pereira, L.F.C., Rabczuk, T., 2019. Outstanding strength, optical characteristics and thermal conductivity of graphene-like BC_3 and BC_6N semiconductors. Carbon 149, 733–742. https://doi.org/10.1016/j.carbon.2019.04.084.

[25] Zahedi, R.K., Shirazi, A., Alimouri, P., Alajlan, N., Rabczuk, T., 2019. Mechanical properties of graphene-like BC_3: a molecular dynamics study. Comput. Mater. Sci. 168, 1–10. https://doi.org/10.1016/j.commatsci.2019.05.053.

[26] Plimpton, S., 1995. Fast parallel algorithms for short-range molecular dynamics. J. Comput. Phys. 117, 1–19. https://doi.org/10.1006/jcph.1995.1039.

[27] Thompson, A.P., Aktulga, H.M., Berger, R., Bolintineanu, D.S., Brown, W.M., Crozier, P.S., et al., 2022. LAMMPS – a flexible simulation tool for particle-based materials modeling at the atomic, meso, and continuum scales. Comput. Phys. Commun. 271, 108171. https://doi.org/10.1016/j.cpc.2021.108171.

[28] Kınacı, A., Haskins, J.B., Sevik, C., Çağın, T., 2012. Thermal conductivity of BN-C nanostructures. Phys. Rev. B 86, 115410. https://doi.org/10.1103/PhysRevB.86.115410.

[29] Stukowski, A., 2010. Visualization and analysis of atomistic simulation data with OVITO – the open visualization tool. Model. Simulat. Mater. Sci. Eng. 18, 015012. https://doi.org/10.1088/0965-0393/18/1/015012.

[30] Hirel, P., 2015. Atomsk: a tool for manipulating and converting atomic data files. Comput. Phys. Commun. 197, 212–219. https://doi.org/10.1016/j.cpc.2015.07.012.

[31] Fereidoon, A., Ahangari, M.G., Ganji, M.D., Jahanshahi, M., 2012. Density functional theory investigation of the mechanical properties of single-walled carbon nanotubes. Comput. Mater. Sci. 53, 377–381. https://doi.org/10.1016/j.commatsci.2011.08.007.

[32] Sha, Z., Quek, S., Pei, Q., Liu, Z., Wang, T., Shenoy, V., Zhang, Y., 2014. Inverse pseudo hall-petch relation in polycrystalline graphene. Sci. Rep. 4, 5991. https://doi.org/10.1038/srep05991.

[33] Jam, A.N., Abadi, R., Izadifar, M., Rabczuk, T., 2018. Molecular dynamics study on the mechanical properties of carbon doped single-layer polycrystalline boron-nitride nanosheets. Comput. Mater. Sci. 153, 16–27. https://doi.org/10.1016/j.commatsci.2018.06.011.

[34] Dadrasi, A., Albooyeh, A., Fooladpanjeh, S., Salmankhani, A., Hamed Mashhadzadeh, A., Saeb, M.R., 2022. Theoretical examination of the fracture behavior of BC_3 polycrystalline nanosheets: effect of crack size and temperature. Mech. Mater. 165, 104158. https://doi.org/10.1016/j.mechmat.2021.104158.

[35] de Sousa, J.M., Botari, T., Perim, E., Bizao, R.A., Galvao, D.S., 2016. Mechanical and structural properties of graphene-like carbon nitride sheets. D. S RSC Adv. 6, 76915–76921. https://doi.org/10.1039/C6RA14273G.

[36] Han, J., Sohn, D., Woo, W., Kim, D.K., 2017. Molecular dynamics study of fracture toughness and trans-intergranular transition in bi-crystalline graphene. Comput. Mater. Sci. 129, 323–331. https://doi.org/10.1016/j.commatsci.2016.12.023.

[37] Bhattacharjee, A., Jiang, H., Li, L.H., Huang, S., Chen, Y.I., Cai, Q., 2024. Thermal transport property of boron nitride nanosheets. Appl. Phys. Rev. 11, 041401. https://doi.org/10.1063/5.0213741.

[38] Xu, B., Wang, H., 2019. Electronic and mechanic properties of a new cubic boron nitride. Comput. Mater. Sci. 162, 111–115. https://doi.org/10.1016/j.commatsci.2019.02.034.

[39] Han, J., Sohn, D., Woo, W., Kim, D.-K., 2017. Molecular dynamics study of fracture toughness and trans-intergranular transition in bi-crystalline graphene. Comput. Mater. Sci. 129, 323–331. https://doi.org/10.1016/j.commatsci.2016.12.023.

[40] Bhattacharjee, A., Jiang, H., Li, L.H., Huang, S., Chen, Y.I., Cai, Q., 2024. Thermal transport property of boron nitride nanosheets. Appl. Phys. Rev. 11, 041401. https://doi.org/10.1063/5.0213741.

[41] Yuan, X., Lin, G., Wang, Y., 2016. Mechanical properties of armchair silicene nanoribbons with edge cracks: a molecular dynamics study. Mol. Simul. 42, 1157–1164. https://doi.org/10.1080/08927022.2016.1148266.

[42] Zhao, H., Aluru, N.R., 2010. Temperature and strain-rate dependent fracture strength of graphene. J. Appl. Phys. 108, 064321. https://doi.org/10.1063/1.3488620.